

Berndt et al.: Rifting under steam

1 Rifting under steam – how rift magmatism triggers  
2 methane venting from sedimentary basins

3 **C. Berndt<sup>1</sup>, C. Hensen<sup>1</sup>, C. Mortera-Gutierrez<sup>2</sup>, S. Sarkar<sup>1</sup>, S. Geilert<sup>1</sup>, M.  
4 Schmidt<sup>1</sup>, V. Liebetrau<sup>1</sup>, R. Kipfer<sup>3,7</sup>, F. Scholz<sup>1</sup>, M. Doll<sup>4</sup>, S. Muff<sup>1</sup>, J. Karstens<sup>1</sup>,  
5 S. Planke<sup>5</sup>, S. Petersen<sup>1</sup>, C. Böttner<sup>1</sup>, W.-C. Chi<sup>6</sup>, M. Moser<sup>1</sup>, R. Behrendt<sup>1</sup>, A.  
6 Fiskal<sup>1</sup>, M.A. Lever<sup>7</sup>, C.-C. Su<sup>8</sup>, L. Deng<sup>7</sup>, M.S. Brennwald<sup>3</sup>, and D. Lizarralde<sup>9</sup>**

7 <sup>1</sup>*GEOMAR Helmholtz Centre for Ocean Research Kiel, Wischhofstr. 1-3, 24148 Kiel,*  
8 *Germany*

9 <sup>2</sup>*Instituto de Geofísica, UNAM, Circuito Exterior, Cd. Universitaria, Coyoacán, D.*  
10 *F., C. P. 04510, Mexico*

11 <sup>3</sup>*Department Water Resources and Drinking Water, Eawag, Überlandstrasse 133,*  
12 *8600 Dübendorf and Noble Gas Laboratory, Institute of Geochemistry and Petrology,*  
13 *ETH, 8092 Zürich, Switzerland.*

14 <sup>4</sup>*Fachbereich Geowissenschaften, Universität Bremen, Leobener Str., 28359 Bremen,*  
15 *Germany*

16 <sup>5</sup>*Volcanic Basin Petroleum Research AS, Gaustadalleen 21, 0349 Oslo, Norway*

17 <sup>6</sup>*Institute of Earth Sciences, Academia Sinica, 128 Academia Rd, Sec.2, Nangang,*  
18 *Taipei, Taiwan*

19 <sup>7</sup>*Department of Environmental Systems Sciences, ETH, Universitätstrasse 16*  
20 *8092 Zürich, Switzerland*

21 <sup>8</sup>*Institute of Oceanography, National Taiwan University, No.1, Sec. 4, Roosevelt*  
22 *Road, Taipei 106, Taiwan*

23 <sup>9</sup>*Woods Hole Oceanographic Institution, Woods Hole, MA 02543-1050 U.S.A.*

24

25

26

27 **ABSTRACT**

28       During opening of a new ocean magma intrudes into the surrounding  
29 sedimentary basins. Heat provided by the intrusions matures the host rock creating  
30 metamorphic aureoles potentially releasing large amounts of hydrocarbons. These  
31 hydrocarbons may migrate to the seafloor in hydrothermal vent complexes in  
32 sufficient volumes to trigger global warming, e.g. during the Paleocene Eocene  
33 Thermal Maximum (PETM). Mound structures at the top of buried hydrothermal vent  
34 complexes observed in seismic data off Norway were previously interpreted as mud  
35 volcanoes and the amount of released hydrocarbon was estimated based on this  
36 interpretation. Here, we present new geophysical and geochemical data from the Gulf  
37 of California suggesting that such mound structures could in fact be edifices  
38 constructed by the growth of black-smoker type chimneys rather than mud volcanoes.  
39 We have evidence for two buried and one active hydrothermal vent system outside the  
40 rift axis. The vent releases several hundred degrees Celsius hot fluids containing  
41 abundant methane, mid-ocean-ridge-basalt (MORB)-type helium, and precipitating  
42 solids up to 300 m high into the water column. Our observations challenge the idea  
43 that methane is emitted slowly from rift-related vents. The association of large  
44 amounts of methane with hydrothermal fluids that enter the water column at high  
45 pressure and temperature provides an efficient mechanism to transport hydrocarbons  
46 into the water column and atmosphere, lending support to the hypothesis that rapid  
47 climate change such as during the PETM can be triggered by magmatic intrusions into  
48 organic-rich sedimentary basins.

49

50

51

## 52 **INTRODUCTION**

53 When testing climate models by hind casts for past prominent warming events it has  
54 become clear that significant drivers are missing (Panchuk et al., 2008; Carozza et  
55 al., 2011). Most striking, the reason for a 5-6°C global warming during the PETM  
56 remains elusive, although it is clear that more than 2000 Gt of carbon must have  
57 entered the atmosphere within a relatively short time span of a few thousand years  
58 (Dickens et al., 1995; Zachos et al., 2001). Light carbon isotope ratios were  
59 interpreted to suggest that large amounts of biogenic carbon were released through  
60 run-away hydrate dissociation events (Kennett et al., 2000). But recent studies call  
61 this interpretation in question (Dickens, 2011; Biastoch et al., 2011). Most  
62 alternative explanations are also marred by contradictions with available data  
63 (Higgins and Schrag, 2006). This includes the hypothesis of carbon mobilization by  
64 magmatic intrusions into carbon-rich continental margin sediments during the  
65 opening of the North Atlantic (Svensen et al., 2004), because it is difficult to  
66 understand how this process could have injected large amounts of carbon into the  
67 atmosphere within a short time.

68

## 69 **THE ACTIVE HYDROTHERMAL MOUND IN THE GUAYMAS BASIN**

70 New data acquired in the Guaymas Basin (Fig. 1, S1) support the ‘tectonic-magmatic’  
71 explanation for warming during the PETM. Our data show a 1050 m-wide and 100 m-  
72 high mound located above thick sediments approximately 1 km southeast of the  
73 northern rift axis of the Guaymas Basin that is emitting carbon-rich hydrothermal  
74 fluids (Fig. 2a). The mound and most of the southern flank of the Guaymas rift valley

75 are underlain by an approximately 100 m-thick chaotic seismic facies (50 to 150 ms  
76 two-way-travel time (TWT)) that is part of a widespread mass transport deposit. In the  
77 area of the mound another chaotic and low seismic amplitude seismic facies continues  
78 further downward to at least 2900 ms TWT or approximately 200-250 metres below  
79 seafloor. We interpret this facies as a conduit for the ascending hydrothermal fluids.  
80 At this depth high seismic amplitude reflections extend southward from below the rift  
81 axis into the basin. These reflections are likely caused by magmatic intrusions which  
82 occur throughout the Guaymas Basin (Lizarralde et al., 2010). The bathymetric data  
83 (Fig. 1) also show the trace of a NE-SW striking normal fault that stretches to the  
84 mound and is dipping westward (Fig. S2). As it strikes in the same direction as the  
85 elongate mound axis it is probable that the shape of the mound is controlled by this  
86 fault. An approximately 20 m-thick chaotic seismic facies immediately below the base  
87 of the mound may indicate that hydrothermal seepage was initially occurring over a  
88 broader area and became more focused once fluid pathways had formed. The up to  
89 30°-steep flanks of the mound suggest a high internal angle of repose of the mound-  
90 forming material.

91

92 A 2.2 km-long profile of ten heat flow stations across the vent field and a 0.4 km-long  
93 profile of five stations along the mound consistently show heat flow values larger than  
94 0.3 W/m<sup>2</sup>. The maximum heat flow on top of the mound is heterogeneous with values  
95 exceeding 10 W/m<sup>2</sup>, whereas values below 3W/m<sup>2</sup> were measured only 100 m away  
96 from the center (Supplementary Table S1). This heat flow pattern is similar to the heat  
97 flow distribution at sediment-free mid ocean ridges (Rona et al., 1996). The strong  
98 lateral heat flow variations indicate focused heat transport by hydrothermal fluids  
99 within narrow fluid pathways.

100

101 Samples recovered from the top of the mound show porous Fe-rich sulfides (Fig. S3)  
102 consisting predominantly of a boxwork of pyrrhotite crystals with minor pyrite, and  
103 marcasite, and rare Zn- and Cu-sulfides (e.g. sphalerite, chalcopyrite, isocubanite).  
104 These are accompanied by a small fraction of non-sulfide minerals (e.g., carbonates,  
105 opal-A and secondary Fe-oxyhydroxides). The mineralogy makes the samples from  
106 the northern rift axis similar to the massive sulfides recovered from the southern  
107 Guaymas Basin (Koski et al., 1985; Peter and Scott, 1988). However, they lack the  
108 abundant petroleum found in the southern rift samples. In analogy to black smoker  
109 deposits from Escanaba Trough the observed mineral assemblage suggests formation  
110 temperatures in the range of 270-330°C (Zierenberg et al., 1993).

111

## 112 **TIMING OF HYDROTHERMAL ACTIVITY**

113 A 5m-long gravity core was taken ~500 m away from the hydrothermal vent field  
114 (Fig. 3). The upper 4 m of the core consist of organic-rich, hemipelagic diatomaceous  
115 clay that is typical for most of Guaymas Basin (Damm et al., 1984). By contrast, the  
116 lowermost 1 m of core consists of coarse-grained hydrothermal deposits intercalated  
117 with clay lenses suggesting the mound to consist of hydrothermal deposits. Given Pb-  
118 210-based sedimentation rates of 0.74 m/kyr inside the hydrothermal vent field  
119 (Station 40) and of 0.79 m/kyr just outside the hydrothermal vent field along the  
120 Northern Guaymas rift axis (Station 66), the hydrothermal deposits are likely 5 to 6  
121 kyr old. This is a minimum age estimate as older hydrothermal material likely exists  
122 below and towards the centre of the vent complex. However, we note that sill  
123 intrusions quickly cool off after emplacement (Jamtveit et al., 2004) and even thick

124 intrusions can only sustain hydrothermal systems for a few kyr. Thus, we infer that  
125 the mound structure must have formed during the last 5-10 kyr.

## 126 **ORIGIN OF THE HYDROTHERMAL FLUIDS**

127 We collected sea water in the vicinity of the hydrothermal field (Fig. 3) with Niskin  
128 bottles and measured the dissolved gases with an adapted membrane-inlet mass-  
129 spectrometer (MIMS (Mächler et al., 2012)). The water is strongly enriched in helium  
130 (He) relative to the atmospheric equilibrium conditions (Fig. S5). At the flanks and  
131 the bottom of the rift valley He concentrations are similar to the concentrations found  
132 in the southern part of the Guaymas Basin (Lupton, 1979) whereas He in the water just  
133 above the active smokers is supersaturated by more than a factor of 4 (Fig. S6). This  
134 enrichment indicates that the vent injects He directly into the water column. The  
135 injected He is strongly enriched in  $^3\text{He}$ . The  $^3\text{He}/^4\text{He}$  ratio ( $10.8 \cdot 10^{-6}$ , Fig. S6, Tab. S3)  
136 agrees with that of excess He from the southern part of the Guaymas Basin (Lupton,  
137 1979) pointing to the same general MORB source, and confirms that water circulation  
138 in the Guaymas Basin distributes He-rich water from the black smoker region  
139 throughout the basin (Marinone, 2003).

140

141 Dissolved concentration of light hydrocarbons determined in water sampled at the  
142 smoker field (Fig. 3) by Niskin bottles are highly enriched (factor  $\geq 10^5$ ) compared to  
143 bottom water concentrations (Tab. S2). Calculated end member concentrations (i.e.  
144  $\text{CH}_4 = 6.5 \text{ mM}$ ; Fig. S7) are similar to that of vent fluids measured in the Southern  
145 Guaymas Basin. There,  $\text{CH}_4$  generation was related to thermocatalytic degradation of  
146 organic matter in sediments intruded by magmatic rocks ( $\text{CH}_4 \sim 6.3 \text{ mM}$ ,  $\text{C1/C2+}$   
147  $\sim 80$ ) (Welhan and Lupton, 1987). The isotopic composition of methane ( $\delta^{13}\text{C} : -39$  to -  
148  $14.9 \text{ ‰}$ ) at our site also indicates thermogenic methane most likely derived from local

149 sediments, however, with admixture of isotopically heavy methane (Fig. S8). This is  
150 consistent with high enrichment in Rn (Tab. S2). The heaviest  $\delta^{13}\text{C}\text{-CH}_4$  is likely  
151 related to an abiogenic methane source derived from water rock interaction (e.g., East  
152 Pacific Rise-type methane (Welhan and Lupton, 1987)). The presence of abiogenic  
153 hydrocarbon is also supported by the isotopic heavy composition of ethane and  
154 propane (McDermott et al., 2015; Proskurowski et al., 2008) (Fig. S9). Although the  
155 high-temperature aureole at the sill-sediment contact zone appears to be the plausible  
156 source for production of hydrocarbons by hydrothermal alteration of organic matter  
157 and abiogenic hydrocarbon release by hydrothermal alteration of magmatic rocks  
158 (McDermott et al., 2015), our concentration and isotope data do not exclude  $^{13}\text{C}$ -  
159 enrichment of methane by (high-temperature) secondary oxidation within the  
160 sediments (Pan et al., 2006; Biddle et al., 2012). In fact, the strongest methane input  
161 from the smoker vent field exhibits an isotopically light  $\delta^{13}\text{C}$ -trend as it is postulated  
162 for the PETM event (Dickens, 2011), and any subsequent methane oxidation product  
163 would maintain this signal. We note that isotopically-light carbon of biogenic origin  
164 accounts for most of the  $\text{CH}_4$  that is emitted from the black smoker field, despite the  
165 presence of an isotopically-heavy hydrocarbon source of abiogenic, magmatic origin.  
166 Thus, we conclude that magmatic activity acts mainly as the heat source that fosters  
167 and triggers  $\text{CH}_4$  production and release from the post-rift sediments. While abiogenic  
168 methane along with MORB-source fluids is indeed emitted, it amounts only to a  
169 minor share of the total liberated  $\text{CH}_4$  (mixing ratio:  $1 : 10^2 - 10^4$ , Fig. S8).

170

171 **COMPARISON TO MOUND STRUCTURES ON THE NORTH ATLANTIC**172 **MARGIN**

173 The Guaymas mound resembles positive relief structures on the Paleocene-Eocene  
174 seafloor of the Vøring Basin off mid-Norway that have been interpreted as mud  
175 volcanoes previously (Svensen et al., 2004; Aarnes et al., 2015). Although deeply  
176 buried, the Norwegian mound structures have similar sizes and internal seismic  
177 appearance as the newly discovered active vent structure in the northern Guaymas  
178 Basin. The Norwegian mound structures are characterized by a transparent to  
179 stratified seismic facies confined by a mostly continuous, low-amplitude seismic  
180 reflection (Fig. 2b). The bases of these dome structures also have rugged topography  
181 with decreased seismic amplitudes and they overlie zones of disturbed seismic  
182 reflections with seismic amplitudes different from their host rocks. These seismic  
183 anomalies may indicate sediment alteration during vent activity (Fig. 2b). In addition  
184 to similar dimensions, the Norwegian and Guaymas structures both have very steep  
185 slopes (Fig. 2c) indicating comparable rheological properties which is uncommon  
186 even for the steepest mud volcanoes so far described for marine environments  
187 (Pinheiro et al., 2003). Seismic data are never fully conclusive – however, the striking  
188 morphological similarity and the location of the structures above seismically imaged  
189 fluid pathways indicates that the Guaymas vent may be a suitable analogue for the  
190 structures that formed at the beginning of the PETM. This link points to an important  
191 role of sediment alteration by ascending hydrothermal fluids and mineral precipitation  
192 in the formation of the mounds.

193

## 194 **IMPLICATIONS**

195 Hydrothermal systems injecting hot, CH<sub>4</sub>- and CO<sub>2</sub>-rich fluids high up into the water  
196 column are a much more efficient mechanism for releasing large amounts of carbon  
197 into the atmosphere than mud volcano-style cold seeps. Such focused ‘hot’ input



198 efficiently bypasses microbial benthic filters that may oxidize much of the CH<sub>4</sub> to the  
199 less potent greenhouse gas CO<sub>2</sub>. Even more important is the observation that  
200 hydrothermal systems can inject CH<sub>4</sub> and CO<sub>2</sub> vigorously several hundred meters  
201 high up into the water column. In a shallow marine rift environment such as the North  
202 Atlantic volcanic rifted margins during the PETM (Planke et al., 2000), such gas  
203 plumes may directly reach the atmosphere. Thus, the new observations support the  
204 hypothesis that the PETM was caused by the vigorous and wide spread magmatic  
205 systems of the North Atlantic large igneous province (Svensen et al., 2004) rather  
206 than by large-scale hydrate dissociation.

207

## 208 **ACKNOWLEDGMENTS**

209 This work is being funded by the German Ministry of Science and Education (BMBF)  
210 through the MAKS project. We thank the master and the crew of research vessel  
211 Sonne for their invaluable support during cruise SO241.

212

## 213 **REFERENCES CITED**

- 214 Biastoch, A., Treude, T., Rüpke, L.H., Riebesell, U., Roth, C., Burwicz, E.B., Park,  
215 W., Latif, M., Böning, C.W., Madec, G., and Wallmann, K., 2011, Rising Arctic  
216 Ocean temperatures cause gas hydrate destabilization and ocean acidification:  
217 *Geophysical Research Letters*, v. 38, p. n/a–n/a, doi: 10.1029/2011GL047222.
- 218 Biddle, J.F., Cardman, Z., Mendlovitz, H., Albert, D.B., Lloyd, K.G., Boetius, A., and  
219 Teske, A., 2012, Anaerobic oxidation of methane at different temperature regimes  
220 in Guaymas Basin hydrothermal sediments: *The ISME Journal*, v. 6, p. 1018–  
221 1031, doi: 10.1038/ismej.2011.164.
- 222 Carozza, D.A., Mysak, L.A., and Schmidt, G.A., 2011, Methane and environmental  
223 change during the Paleocene-Eocene thermal maximum (PETM): Modeling the  
224 PETM onset as a two-stage event: *Geophysical Research Letters*, v. 38, p. n/a–  
225 n/a, doi: 10.1029/2010GL046038.
- 226 Damm, Von, K.L., Edmond, J.M., Measures, C.I., and Grant, B., 1984, Chemistry of  
227 submarine hydrothermal solutions at Guaymas Basin, Gulf of California:  
228 *Geochimica et Cosmochimica Acta*, v. 49, p. 2221–2237, doi: 10.1016/0016-

- 229 7037(85)90223-6.
- 230 Dickens, G.R., 2011, Down the Rabbit Hole: toward appropriate discussion of  
 231 methane release from gas hydrate systems during the Paleocene-Eocene thermal  
 232 maximum and other past hyperthermal events: *Climate of the Past*, v. 7, p. 831–  
 233 846, doi: 10.5194/cp-7-831-2011.
- 234 Dickens, G.R., O'Neil, J.R., Rea, D.K., and Owen, R.M., 1995, Dissociation of  
 235 oceanic methane hydrate as a cause of the carbon isotope excursion at the end of  
 236 the Paleocene: *Paleoceanography*, v. 10, p. 965–971.
- 237 Higgins, J.A., and Schrag, D.P., 2006, Beyond methane: Towards a theory for the  
 238 Paleocene-Eocene Thermal Maximum: *Earth and Planetary Science Letters*, v.  
 239 245, p. 523–537, doi: 10.1016/j.epsl.2006.03.009.
- 240 Welhan, J.A. and Lupton, J.E., 1987, Light Hydrocarbon Gases in Guaymas Basin  
 241 Hydrothermal Fluids: Thermogenic Versus Abiogenic Origin: *AAPG Bulletin*, v.  
 242 71, p. 215–223, doi: 10.1306/94886d76-1704-11d7-8645000102c1865d.
- 243 Jamtveit, B., Svensen, H., Podladchikov, Y.Y., and Planke, S., 2004, Hydrothermal  
 244 vent complexes associated with sill intrusions in sedimentary basins, *in*  
 245 *Geological Society of London*, 9 p. p. 233–241.
- 246 Kennett, J.P., Cannariato, K.G., Hendy, I.L., and Behl, R.J., 2000, Carbon Isotopic  
 247 Evidence for Methane Hydrate Instability During Quaternary Interstadials:  
 248 *Science*, v. 288, p. 128–133, doi: 10.1126/science.288.5463.128.
- 249 Koski, R.A., Lonsdale, P.F., Shanks, W.C., Berndt, M.E., and Howe, S.S., 1985,  
 250 Mineralogy and geochemistry of a sediment-hosted hydrothermal sulfide deposit  
 251 from the Southern Trough of Guaymas Basin, Gulf of California: *Journal of*  
 252 *Geophysical Research: Solid Earth*, v. 90, p. 6695–6707, doi:  
 253 10.1029/JB090iB08p06695.
- 254 Lizarralde, D., Soule, S.A., Seewald, J.S., and Proskurowski, G., 2010, Carbon release  
 255 by off-axis magmatism in a young sedimented spreading centre: *Nature*  
 256 *Geoscience*, v. 4, p. 50–54, doi: 10.1038/NGEO1006.
- 257 Lupton, J.E., 1979, Helium-3 in the Guaymas Basin: Evidence for injection of mantle  
 258 volatiles in the Gulf of California: *Journal of Geophysical Research: Solid Earth*,  
 259 v. 84, p. 7446–7452, doi: 10.1029/JB084iB13p07446.
- 260 Marinone, S.G., 2003, A three-dimensional model of the mean and seasonal  
 261 circulation of the Gulf of California: *Journal of Geophysical Research*, v. 108, p.  
 262 3325–27, doi: 10.1029/2002JC001720.
- 263 Mächler, L., Brennwald, M.S., and Kipfer, R., 2012, Membrane Inlet Mass  
 264 Spectrometer for the Quasi-Continuous On-Site Analysis of Dissolved Gases in  
 265 Groundwater: *Environmental Science & Technology*, v. 46, p. 8288–8296, doi:  
 266 10.1021/es3004409.
- 267 McDermott, J.M., Seewald, J.S., German, C.R., and Sylva, S.P., 2015, Pathways for  
 268 abiotic organic synthesis at submarine hydrothermal fields: *Proceedings of the*

- 269 National Academy of Sciences, v. 112, p. 7668–7672, doi:  
270 10.1073/pnas.1506295112.
- 271 Pan, C., Yu, L., Liu, J., and Fu, J., 2006, Chemical and carbon isotopic fractionations  
272 of gaseous hydrocarbons during abiogenic oxidation: *Earth and Planetary Science*  
273 *Letters*, v. 246, p. 70–89, doi: 10.1016/j.epsl.2006.04.013.
- 274 Panchuk, K., Ridgwell, A., and Kump, L.R., 2008, Sedimentary response to  
275 Paleocene-Eocene Thermal Maximum carbon release: A model-data comparison:  
276 *Geology*, v. 36, p. 315–5, doi: 10.1130/G24474A.1.
- 277 Peter, J.M., and Scott, S.D., 1988, Mineralogy, composition, and fluid-inclusion  
278 microthermometry of seafloor hydrothermal deposits in the southern trough of  
279 Guaymas Basin, Gulf of California: *Canadian Mineralogist*.
- 280 Pinheiro, L.M., Ivanov, M.K., Saoutkine, A., Akhmanov, G., Magalhães, V.H.,  
281 Volkonskaia, A., Monteiro, J.H., Somoza, L., Gardner, J.M., Hamouni, N., and  
282 Cunha, M.R., 2003, Mud volcanism in the Gulf of Cadiz: results from the TTR-10  
283 cruise: *Marine Geology*, v. 195, p. 131–151, doi: 10.1016/S0025-3227(02)00685-  
284 0.
- 285 Planke, S., Symonds, P.A., Alvestad, E., and Skogseid, J., 2000, Seismic  
286 volcanostratigraphy of large-volume basaltic extrusive complexes on rifted  
287 margins: *Journal of Geophysical Research*, v. 105, p. 19–335–19–351.
- 288 Proskurowski, G., Lilley, M.D., Seewald, J.S., Früh-Green, G.L., Olson, E.J., Lupton,  
289 J.E., Sylva, S.P., and KeLLey, D.S., 2008, Abiogenic Hydrocarbon Production at  
290 Lost City Hydrothermal Field: *Science*, v. 319, p. 604–607, doi:  
291 10.1126/science.1151194.
- 292 Rona, P.A., Petersen, S., Becker, K., Herzen, Von, R.P., Hannington, M.D., Herzig,  
293 P.M., Naka, J., Lalou, C., and Thompson, G., 1996, Heat flow and mineralogy of  
294 TAG Relict High-Temperature Hydrothermal Zones: Mid-Atlantic Ridge 26°N,  
295 45°W: *Geophysical Research Letters*, v. 23, p. 3507–3510, doi:  
296 10.1029/96gl03257.
- 297 Svensen, H., Planke, S., Malthe-Sørenssen, A., Jamtveit, B., Myklebust, R., Eidem,  
298 T.R., and Rey, S.S., 2004, Release of methane from a volcanic basin as a  
299 mechanism for initial Eocene global warming.: *Nature*, v. 429, p. 542–545, doi:  
300 10.1038/nature02566.
- 301 Zachos, J., Pagani, M., Sloan, L., Thomas, E., and Billups, K., 2001, Trends,  
302 Rhythms, and Aberrations in Global Climate 65 Ma to Present: *Science*, v. 292, p.  
303 686–693, doi: 10.1126/science.1059412.
- 304 Zierenberg, R.A., Koski, R.A., Morton, J.L., and Bouse, R.M., 1993, Genesis of  
305 massive sulfide deposits on a sediment-covered spreading center, Escanaba  
306 Trough, southern Gorda Ridge: *Economic Geology*, v. 88, p. 2069–2098, doi:  
307 10.2113/gsecongeo.88.8.2069.

309

310

311

312

313 **FIGURE CAPTIONS**

314 Figure 1. The Guaymas Basin is one of the rift basins formed by opening of the Gulf  
315 of California in NW-SE direction. The recently discovered black smoker is located  
316 just south of the northern rift axis.

317

318 Figure 2. Comparison of the seismic signature of the active black smoker (a) and an  
319 extinct structure in the Guaymas (b and c) and extinct structures observed in the  
320 Vøring Basin during the opening of the Northeast Atlantic off Norway (d and e).  
321 Width (f) and height (g) of the active black smoker in the Guaymas Basin are similar  
322 to structures in the Vøring Basin as indicated by the red line in the blue histograms.  
323 Green lines, average width and height. MTD, mass transport deposit. CSF, chaotic  
324 seismic facies underneath the smoker. Vertical axis on all seismic images shows two  
325 way travel time in ms.

326

327 Figure 3. Three-dimensional view of the mound structure discovered in the Guaymas  
328 Basin. Station IDs of CTD tracks (green lines), HyBis dives (red lines), gravity core  
329 (yellow triangle), and in situ sensor data ( $p\text{CH}_4$  ( $\mu\text{atm}$ ) /  $p\text{CO}_2$  ( $\mu\text{atm}$ ) / temperature  
330 ( $^{\circ}\text{C}$ )) are labelled.

331

332 Figure 4. Schematic diagram illustrating the processes at the active vent site. The  
333 green area indicates under-mature sediments from which organic carbon can be

334 mobilized by the heat transfer from the magmatic intrusions limiting the depth within  
335 which the bulk of the fluids may originate. MTD: Mass transport deposit.

336

337 <sup>1</sup>GSA Data Repository item 201Xxxx, including supplementary figures and references  
338 as well as additional information on heat flow measurements, geochemical analysis of  
339 sediment pore water and water column samples, determination of the sedimentation  
340 rate and further seismic information, is available online at  
341 [www.geosociety.org/pubs/ft20XX.htm](http://www.geosociety.org/pubs/ft20XX.htm), or on request from [editing@geosociety.org](mailto:editing@geosociety.org) or  
342 Documents Secretary, GSA, P.O. Box 9140, Boulder, CO 80301, USA.

343

344

#### 345 **GSA Data Repository Materials**

346

#### 347 *Seafloor temperature measurements*

348 The temperature gradients were measured using a 5 m-long temperature-gradient  
349 lance with six miniaturized temperature data loggers (MTL). These loggers measured  
350 the temperature at a sampling rate of 1 s with an absolute accuracy of approximately  
351 0.1 K (Pfender and Villinger 2002). The relative temperature resolution is 0.001 K. In  
352 addition, at six sites a 5 m-long gravity corer with attached MTLs was used. An  
353 additional logger at the top of both instruments measured the bottom water  
354 temperature as a reference. All measurements were tilt corrected. The derived  
355 temperature data were not corrected for sedimentation and terrain effects.

356

357 We have measured the thermal conductivity on recovered core material that was  
358 sampled at or close to the depth of the measured temperature positions using the KD2  
359 Pro Needle Probe Instrument. For the samples without a thermal-conductivity

360 measurement, i.e. those without cores, we assumed a constant thermal conductivity of  
361 0.7 W/m K. The data were processed using the method published by Hartmann and  
362 Villinger (2002). This method determines undisturbed sediment temperatures from the  
363 observed temperature decays.

364 Heat flow values were calculated by using Fourier's Law as the product of the  
365 temperature gradient and thermal conductivity.

366

367 We used Bullard method in which the integrated thermal resistance is plotted as a  
368 function of temperature. Usually this relationship is linear. However, transient  
369 processes such as high sedimentation rates, seasonal temperature fluctuations, focused  
370 advection processes or heat generation may cause non-linear deviations. Fourteen out  
371 of the 15 presented heat flow sites show a linear relationship between temperatures as  
372 function of integrated thermal resistance. Just one site shows non-linear relation at  
373 shallow sediment depth.

374

375 We interpret the overall high heat flow values with large lateral variations as a result  
376 of hydrothermal fluid movements along narrow pathways. The high temperature  
377 gradient (Supplementary Table S1) excludes conductive heat transfer. Conductive  
378 heat transfer cannot explain either the large lateral heat flow variations on a spatial  
379 scale of 100 m. This indicates that there is rigorous hydrothermal venting. All of the  
380 SO241-70 sites show advective components. Three out of these four are interpretable  
381 as discharge areas (in the northern and central part of the graben), but the Bullard plot  
382 of (Site SO241-70P04) shows a downward concave curve at shallow depth, which  
383 may be the result of seawater recharge into the crust before it is being heated up.

384

385 ***Geochemistry***

386 Water samples were taken by using a towed SBE9-CTD rosette device equipped with  
387 11 Niskin bottles (a 10 l) and additional HydroC-pCH<sub>4</sub> and -pCO<sub>2</sub>, turbidity, and  
388 bottom distance sensors (modified after Schmidt et al., 2015). CTD-Stations VCTD09  
389 (and -10) were towed directly above the hydrothermal vent field in variable distance  
390 to seafloor (Fig. 3). However, only VCTD09 data is shown in Table S2 as it exhibit  
391 notable inorganic variations of hydrothermal tracers in water masses in 5-20 m  
392 distance to seafloor. Niskin bottles were closed when temperature, pCO<sub>2</sub> and turbidity  
393 suddenly increased indicating hydrothermal plume anomalies. The Niskin bottles  
394 were sub-sampled directly after CTD retrieval for inorganic element chemistry,  
395 nutrients, partial pressures of dissolved gases and stable and radio-isotope  
396 characteristics (Tab. S2) and water samples were analysed onboard for nutrient  
397 concentrations. Sub-samples taken for the analysis of major cations (Na<sup>+</sup>, K<sup>+</sup>, Li<sup>+</sup>,  
398 Mg<sup>2+</sup>, Ca<sup>2+</sup>, Sr<sup>2+</sup>, Ba<sup>2+</sup>) as well as B and Si were measured in the shore-based  
399 laboratory at GEOMAR Helmholtz-Centre for Ocean Research by ICP-OES  
400 ([http://www.geomar.de/en/research/fb2/fb2-mg/benthic-biogeochemistry/mg-](http://www.geomar.de/en/research/fb2/fb2-mg/benthic-biogeochemistry/mg-analytik/icp-aes/)  
401 [analytik/icp-aes/](http://www.geomar.de/en/research/fb2/fb2-mg/benthic-biogeochemistry/mg-analytik/icp-aes/)). ICP sub-samples were acidified directly after sampling to prevent  
402 any precipitation of minerals. The elements Ba, Mn, Si, and Li are enriched compared  
403 to seawater values. The concentration ranges between 128 – 1766 nM for Ba, 0.02 to  
404 23.9 µM for Mn, 0.16 – 0.69 mM for Si and 23.1 – 59.2 µM for Li (Table S2). All  
405 elements show the strongest anomalies (mostly enrichment) in bottle 12 (VCTD09).  
406 Mg shows a slight concentration decrease compared to seawater. The strongest  
407 depletion of Mg (51 mM) was also encountered in bottle 12. TIMS measured <sup>87</sup>Sr/<sup>86</sup>Sr  
408 ratios normalized on SRM-987 (0.710248) ranges between 0.708906 and almost

409 modern seawater (0.709176) matching 0.709170 ( $\pm 1 \text{ E-}5$ , typical 2 SEM this session)  
410 showing the lowest value in bottle 12 which was sampled closest to the active vent.

411

412 We calculated the amount of hydrothermal fluids in the Guaymas Basin bottom water  
413 using a simple two-end member mixing model between the seawater and primary  
414 hydrothermal fluid which was assumed to be void of Mg. Based on this we calculated  
415 the maximum percentage of the hydrothermal fluid in the water samples. The lowest  
416 Mg concentration of 51 mM in the water sample of bottle 12 yields a hydrothermal  
417 fluid percentage of ~6 %. Based on this we determined the hydrothermal end member  
418 composition of the enriched elements in the sampled water column and compared  
419 those to the concentrations measured at the southern Guaymas spreading center by  
420 Von Damm et al. (1985).

421

422 Hydrothermal end member concentrations for Si and Ba yielded 9.36 mM and 28  $\mu\text{M}$ ,  
423 respectively and fall well into the end member concentration ranges observed by Von  
424 Damm et al. (1985) in the southern Guaymas Basin (Si: 9 - 14 mM; Ba: 7 – 42  $\mu\text{M}$ ).  
425 Si concentration is at the lower end of the concentration range and might point to a  
426 lower hydrothermal temperature or Si precipitation during ascent or after fluid  
427 discharge. Hydrothermal end member concentrations calculated for Mn yield 420  $\mu\text{M}$ ,  
428 which is higher than the concentrations observed in the southern Guaymas  
429 hydrothermal fluids, which range between 128 and 236  $\mu\text{M}$  (Von Damm et al., 1985).  
430 Von Damm et al. (1985) propose the precipitation of alabandite (MnS) as an  
431 explanation for the observed low values. Li, in contrast, shows slightly lower  
432 calculated end member concentrations (584  $\mu\text{M}$ ) compared to the southern Guaymas  
433 fluids, which range between 630 and 1076  $\mu\text{M}$ . These lower values might be



434 explained by a Li sink in the sediments through which the hydrothermal fluids  
435 percolate.

436

437 Concentrations of dissolved He and Ne (as well as Ar, Kr and Xe) and the  $^3\text{He}/^4\text{He}$ ,  
438  $^{22}\text{Ne}/^{20}\text{Ne}$ ,  $^{36}\text{Ar}/^{40}\text{Ar}$  isotope ratios in water samples taken in copper tubes were  
439 analysed as routine samples in the noble gas laboratory of the Swiss Federal Institute  
440 of Technology Zurich (ETHZ) and the Swiss Federal Institute of Aquatic Science and  
441 Technology (Eawag). Details on sampling and of the experimental method are given  
442 in Beyerle et al. (2000). He and Ne concentrations are covered with an overall  
443 standard error of  $\pm 2\%$ , the  $^3\text{He}/^4\text{He}$  ratio has a standard error of 1%.

444

445 For the on-board analysis concentrations of dissolved He, Ar, Kr,  $\text{N}_2$ ,  $\text{O}_2$ ,  $\text{CO}_2$ , and  
446  $\text{CH}_4$  during the expedition, we used a portable gas-equilibrium membrane-inlet mass-  
447 spectrometric system (GE-MIMS) similar to that described in Mächler et al. (2012).  
448 Whereas the original GE-MIMS was designed for gas analysis in continuous high-  
449 volume water flows through a large membrane contactor, the GE-MIMS used here  
450 was modified to allow analysis of an 8 l water sample taken from a 10 l Niskin  
451 sampler within 10 min (Brennwald et. al., 2015, a, b). To allow reliable gas analysis  
452 in this limited amount of water, the gas consumption from the membrane contactor  
453 into of the MS was reduced to 0.1 ccSTP/min ( $> 2$  ccSTP/min in the original GE-  
454 MIMS). This allowed maintaining gas/water solubility equilibrium in miniature  
455 membrane contactor modules (two LiquiCel MicroModules operated in parallel) at a  
456 total water throughput of 0.5 L/min ( $> 5$  L/min in the original GE-MIMS). The low  
457 gas consumption was achieved by replacing the capillary flow resistance followed by  
458 a split-flow/aperture gas inlet to the MS vacuum by a new splitless design using a

459 single capillary (9 m long, 0.1 mm inner diameter, Brennwald et al., 2015b). The gas  
460 outflow from the capillary is analysed in a quadrupole MS (Stanford Research  
461 Systems RGA 200) operated in dynamic mode. As the membrane contactors operate  
462 at solubility equilibrium, the partial pressures of the noble gases N<sub>2</sub> and O<sub>2</sub> in the gas  
463 phase of the membrane contactors are similar to those in air. The GE-MIMS data for  
464 these species were therefore calibrated using ambient air as a reference gas (< 5 %  
465 accuracy, 1  $\sigma$ ). The partial pressures of CO<sub>2</sub> and CH<sub>4</sub> are reported as un-calibrated  
466 raw data.

467

468 In order to determine the variation of excess amounts of the noble gas radon  
469 (<sup>222</sup>Rn<sub>(exc.)</sub>) close to the hydrothermal vent, selected CTD samples were measured on  
470 board by Liquid Scintillation Counting (LSC). Using a portable Hidex Triathler™  
471 system and MaxiLight™ as scintillation cocktail for the measurement of total <sup>222</sup>Rn  
472 content uncertainties of 15% (SD) are typical for the counting statistics. After more  
473 than 3 months storage re-measurements were conducted at GEOMAR to correct for  
474 the fraction of total <sup>222</sup>Rn potentially provided by the decay of dissolved <sup>226</sup>Ra. The  
475 analytical procedure followed the approach described by Purkl and Eisenhauer  
476 (2004). The maximum sample size was restricted to 1.5 l combined with 20 ml of  
477 LSC cocktail, which is close to the maximum extraction efficiency as recently  
478 deduced by Schubert et al. (2014). The re-measurements for supported <sup>222</sup>Rn  
479 contribution did not reveal concentrations above the detection limit of the applied  
480 LSC setup. Consequently, a simple, robust, and reliable semi-quantitative measure on  
481 the relative enrichment in <sup>222</sup>Rn<sub>(exc.)</sub> can be presented in Tab. S2 in terms of  
482 enrichment factors compared to bottle 5. Since bottle 5 shows the lowest <sup>222</sup>Rn  
483 activity in dpm/L (decay per minute/liter) of the investigated CTD casts it provides

484 the best available approximation to water column background  $^{222}\text{Rn}$  activity and was  
485 set as reference point (Tab. S2). The lowest published  $^{222}\text{Rn}$  data (0.1 and 0.2 dpm/L)  
486 of Santos et al. (2011) for central waters of the Concepcion Bay (West of our study  
487 area) and of Prol-Ledesma et al. (2013) for the northern Gulf of California (Wagner  
488 and Consag basins, down to zero dpm/100L) may be assumed as typical background  
489 values and are similar to the lowest values that we have encountered (bottle 5, 1768  
490 m: 0.17 dpm/L ( $\pm 0.1$ , SD; calibration pending). However, applying the same  
491 approach to the sample recovered closest to the vent (bottle 12, 1773 m) yielded the  
492 maximum  $^{222}\text{Rn}_{(\text{exc.})}$  activity of 13.8 dpm/L for our data set. Independent from exact  
493 quantitative setup calibrations, this approach provides a robust enrichment factor for  
494  $^{222}\text{Rn}_{(\text{exc.})}$  in the same order of magnitude as deduced for He in this study (Tab. S2).  
495 However, almost twice as high levels of  $^{222}\text{Rn}_{(\text{exc.})}$  of 2430 dpm/100L were reported  
496 for the hydrothermal impact on the waters of the northern Gulf of California in the  
497 Wagner and Consag basins (Prol-Ledema et al., 2013). There they attribute the  
498 positive anomalies of  $^{222}\text{Rn}$  to a fault system coinciding with the presence of strong  
499 flares suggesting hydrothermal circulation in a thick sediment cover and revealing the  
500 location of up-flow areas.

501

502 Dissolved hydrocarbons (C1-C3) from individual water samples were released  
503 onboard by equilibration of 112 ml water samples in a septum-sealed 117 ml  
504 headspace vial at room temperature (He-head space, 50  $\mu\text{l}$   $\text{HgCl}_2$ -solution added).  
505 Hydrocarbon composition of the head space gas was determined by using a Thermo  
506 Trace gas chromatograph (GC) equipped with flame ionization detector (carrier gas:  
507 He 5.0; capillary column: RT Alumina Bond-KCl, column length: 50 m; column  
508 diameter: 0.53  $\mu\text{m}$ ). Precision of  $\pm 1$ -3% was achieved when measuring standard

509 hydrocarbon mixtures. Molar hydrocarbon concentrations in Table S2 were calculated  
510 by applying Henry coefficients according to Mackay and Shiu (2006).

511

512 Stable carbon isotope ratios of methane and higher hydrocarbons (C1-C3) from water  
513 samples were measured by using continuous flow GC combustion - Isotope Ratio  
514 Mass Spectrometry. Hydrocarbons were separated in a Thermo Trace GC (carrier gas:  
515 He; packed column: ShinCarbon, 1.5 m). The subsequent conversion of hydrocarbons  
516 to carbon dioxide was conducted in a Ni/Pt combustion furnace at 1150°C. The  
517  $^{13}\text{C}/^{12}\text{C}$ -ratios of the produced  $\text{CO}_2$  were determined by a Thermo MAT253 isotope  
518 ratio mass spectrometer. All isotope ratios are reported in the  $\delta$ -notation with respect  
519 to Vienna Pee Dee Belemnite (VPDB, analytical precision 0.5 ‰).

520

### 521 *Sedimentation Rates*

522 The wet sediment was weighed, freeze dried at -80°C and reweighed to determine the  
523 water content, then ground in a mortar. Radionuclides were then measured as follows.  
524 Two HPGe detectors were engaged for  $^{210}\text{Pb}$  and  $^{226}\text{Ra}$  analysis including GMX-type  
525 (ORTEC GMX-120265) and well-type (ORTEC GWL-100230) detectors which  
526 interfaced to a digital gamma-ray spectrometer (DSpecPlus™). For the GMX-type  
527 detector, absolute counting efficiencies for various photon energies were calibrated  
528 using IAEA reference materials 327A, 444 spiked soil, CU-2006-03 spiked soil,  
529 RGTh and RGU for sample weight at 100g as a reference, and coupled with an in-  
530 house secondary standard for various masses (from 10 to 250 g) to calibrate the effect  
531 of sample mass on the attenuation of  $\gamma$ -rays of various energies. For the well-type  
532 detector, the counting efficiencies were calibrated by IAEA-RGTh and RGU from 0.5  
533 to 3.5 g.  $^{214}\text{Pb}$  was used as an index of  $^{226}\text{Ra}$  (supported  $^{210}\text{Pb}$ ) whose activity

534 concentration was subtracted from that of the measured total  $^{210}\text{Pb}$  to obtain excess  
535  $^{210}\text{Pb}$  ( $^{210}\text{Pb}_{\text{ex}}$ ). The  $^{210}\text{Pb}$  and  $^{214}\text{Pb}$  activities were quantified based on photon peaks  
536 centered at 46.52 and 351.99 keV, respectively. The activities of radionuclides were  
537 decay-corrected to the date of sample collection. All radionuclide data were calculated  
538 on salt-free dry weight basis. Error bars represent  $\pm 1\sigma$  around the mean based on  
539 counting statistics and standard propagation of errors.

540

541 ***Supplementary references not in the main manuscript***

542 Beyerle, U., Aeschbach-Hertig, W., Imboden, D. M., Baur, H., Graf, T., Kipfer, R.  
543 (2000) A mass spectrometric system for the analysis of noble gases and tritium  
544 from water samples. *Env. Sci. Technol.*, 34, 2042-2050.

545 Brennwald, M.S., Rüssel, R., Kipfer, R. (2015a) Recent advances in the on-site  
546 analysis and process-based interpretation of dissolved (noble) gases in water  
547 bodies. *Goldschmidt Abstracts*, 386.

548 Brennwald, M.S., Rüssel, R., Kipfer, R. (2015b) Landing (noble) gas analytics in the  
549 field: towards real time insitu gas determination. *Goldschmidt Abstracts*, 387.

550 Des Marais, D. J., Stallard, M. L., Nehring, N. L. & Truesdell, A.H. Carbon isotope  
551 geochemistry of hydrocarbons in Cerro Prieto geothermal field, Baja California  
552 Norte, Mexico. *Chemical Geology* **71**, 159–167, 1988.

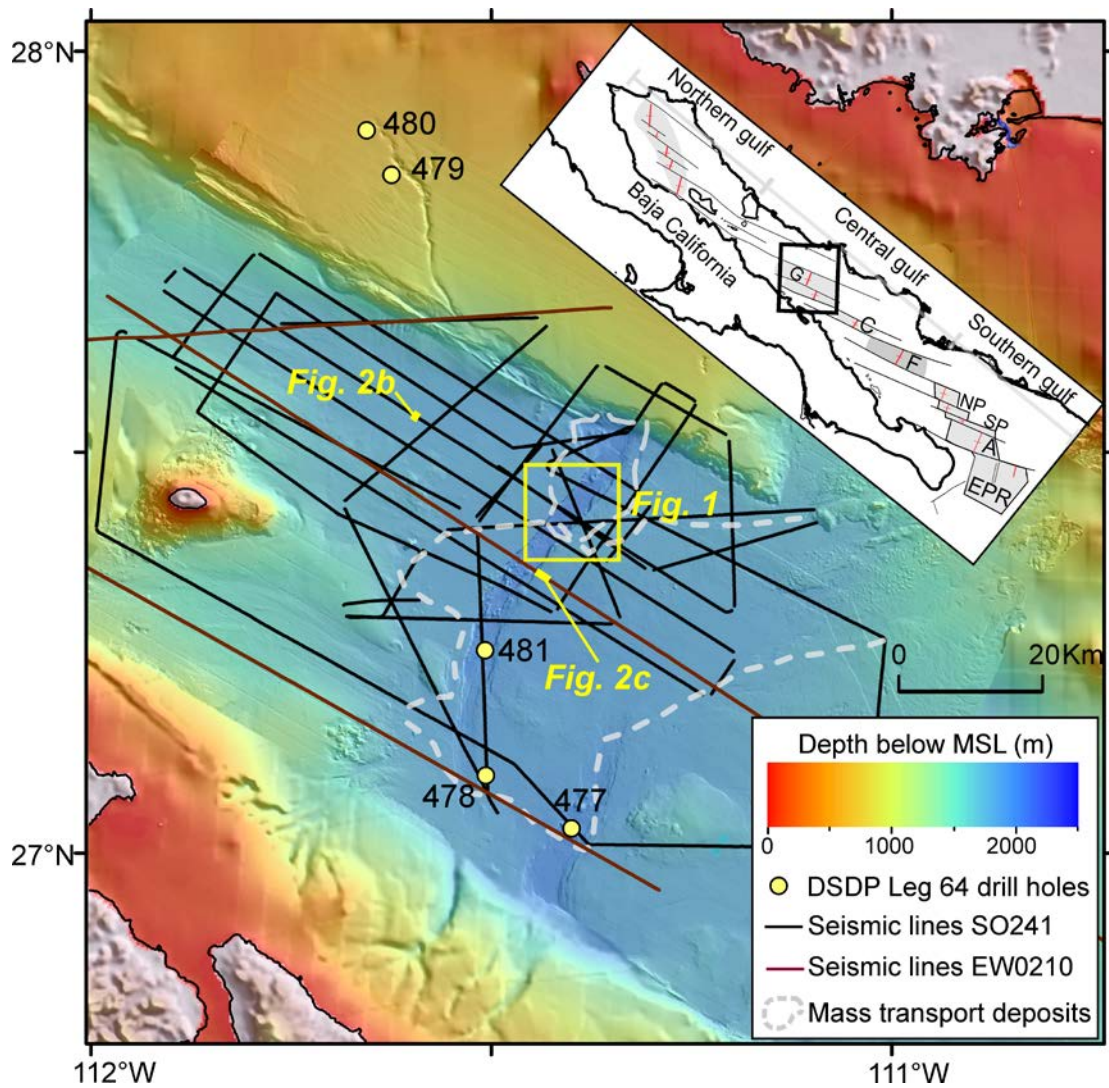
553 Hartmann A, Villinger H (2002) Inversion of marine heat flow measurements by  
554 expansion of the temperature decay function. *Geophysical Journal International*  
555 148 (3): 628-636. doi:10.1046/j.1365-246X.2002.01600.x

556 Lupton, J. E. (1979) Helium-3 in the Guaymas Basin: evidence for injection of mantle  
557 volatiles in the Gulf of California, *Journal of Geophysical Research* 84:  
558 7464.7452.

- 559 Mackay, D. & Shiu, W. Y. A critical review of Henry's law constants for chemicals  
560 of environmental interest. *J. Phys. Chem. Ref. Data* **10** (4), 1175–1199 (2006).
- 561 Mächler, L., Brennwald, M. S., and Kipfer, R. (2012) Membrane inlet mass  
562 spectrometer for the quasi-continuous on-site analysis of dissolved gases in  
563 groundwater. *Environmental Science and Technology* 46: 8288-8296.
- 564 Padilla y Sánchez, R.J., Domínguez Trejo, I., López Azcárraga, A.G., Mota Nieto, J.,  
565 Fuentes Menes, A.O., Rosique Naranjo, F., Germán Castelán, E.A., Campos  
566 Arriola, S.E., 2013, National Autonomous University of Mexico Tectonic Map of  
567 Mexico GIS Project, American Association of Petroleum Geologists GIS Open  
568 Files series.
- 569 Pfender M, Villinger H (2002) Miniaturized data loggers for deep sea sediment  
570 temperature gradient measurements. *Marine Geology* 186: 557-570
- 571 Prol-Ledesma R.M., Torres-Vera M.A., Rodolfo-Metalpa R., Ángeles C., Lechuga  
572 Deveze C.H., Villanueva-Estrada R.E., Shumilin E. and Robinson C. (2013) High  
573 heat flow and ocean acidification at a nascent rift in the northern Gulf of  
574 California. *Nature Communications*, DOI: 10.1038/ncomms2390.
- 575 Purkl S. and Eisenhauer, A. (2004) Determination of Radium Isotopes and  $^{222}\text{Rn}$  in a  
576 groundwater affected coastal area of the Baltic Sea and the underlying sub-sea  
577 floor aquifer. *Marine Chemistry*, 87 . pp. 137-149.
- 578 Santos I., Lechuga-Deveze C., Peterson R.N. and Burnett W.C. (2011) Tracing  
579 submarine hydrothermal inputs into a coastal bay in Baja California using radon.  
580 *Chemical Geology*, 282, pp. 1-10.
- 581 Schmidt, M., Linke, P., Sommer, S., Esser, D. & Cherednichenko, S. Natural CO<sub>2</sub>  
582 seeps offshore Panarea – A test site for subsea CO<sub>2</sub> leak detection technology.  
583 *Marine Technology Society Journal* **49** (1), 19-30 (2015).

- 584 Schubert M., Kopitz J. and Chalupnik S. (2014) Sample volume optimization for  
585 radon-in-water detection by liquid scintillation counting. *Journal of Environmental*  
586 *Radioactivity*, 134, pp. 109-113.
- 587 Von Damm, K. L., Edmond, J. M., Measures, C. I., Grant, B. (1985) Chemistry of  
588 submarine hydrothermal solutions at Guaymas Basin, Gulf of California.  
589 *Geochimica Cosmochimica Acta* 49: 2221–2237.

590



591

592

593 Figure S1: Seismic base map showing the distribution of available 2D seismic data in

594 the Guaymas Basin and major structural elements (after Padilla y Sánchez et al.,

595 2013). Central and Southern gulf spreading centers are labelled, G–Guaymas, C–

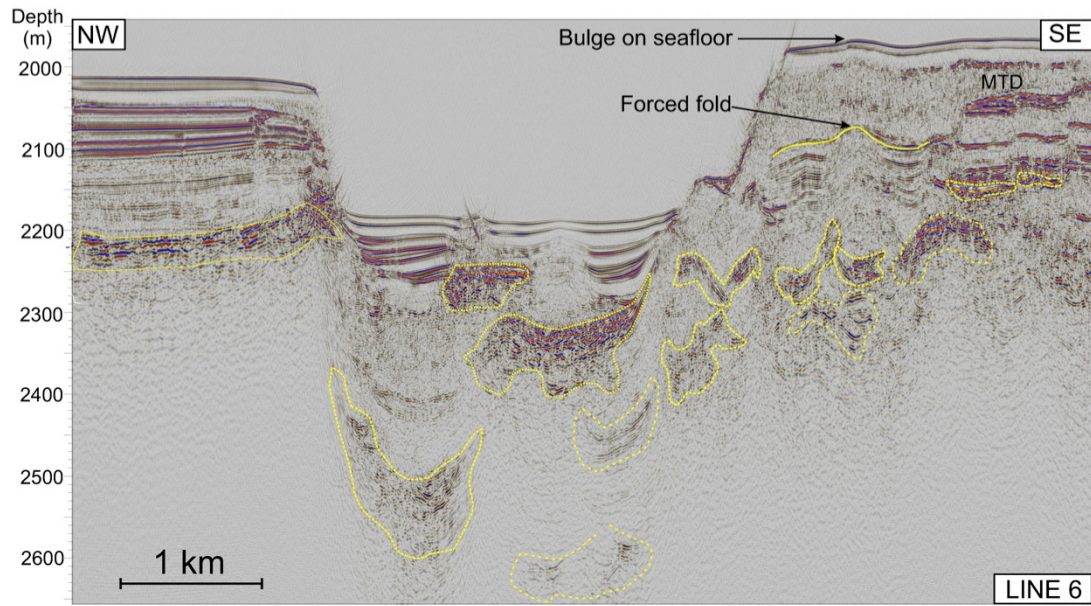
596 Carmen, F–Farallon, NP–North Pescadero, SP–South Pescadero, A–Alarcon, EPR–

597 East Pacific Rise.

598

599





600

601 Figure S2: 2D seismic line showing the regional mass transport deposit (MTD) and  
602 interpreted sill intrusions (yellow polygons).

603

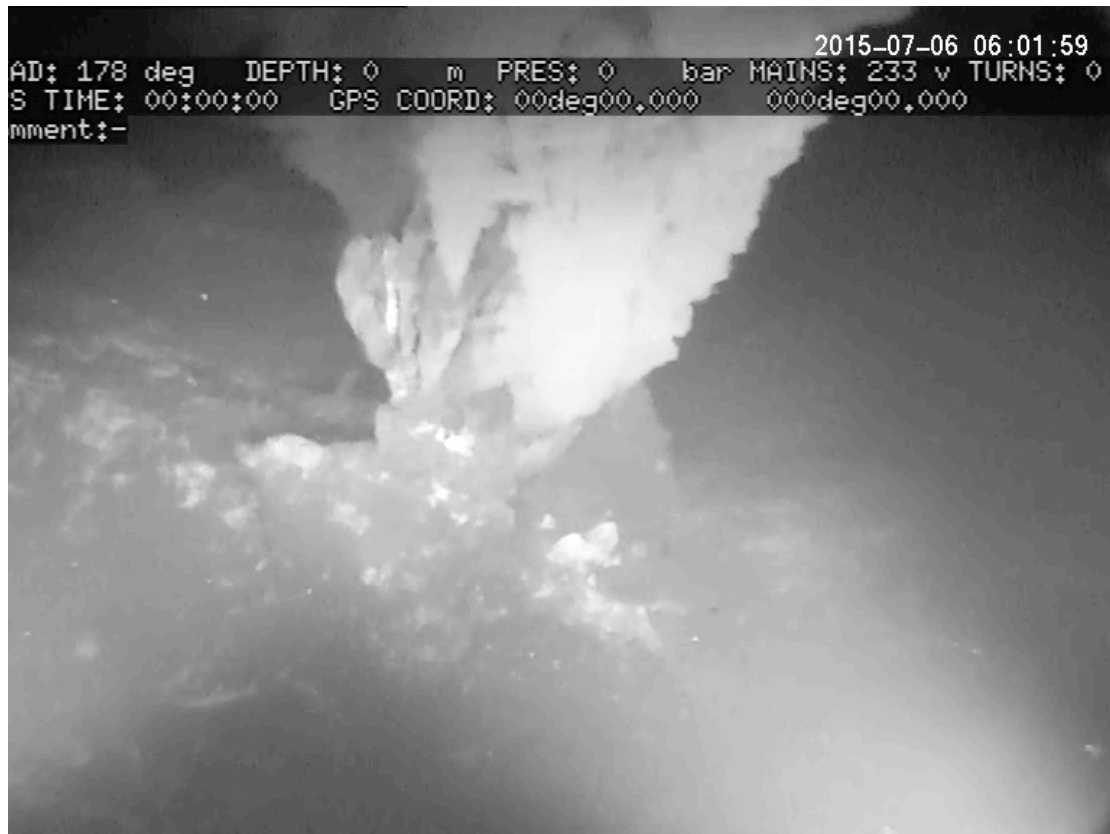
604



605

606 Figure S3: Photograph of a massive sulfide sample collected on the southern summit  
607 of the mound structure.

608

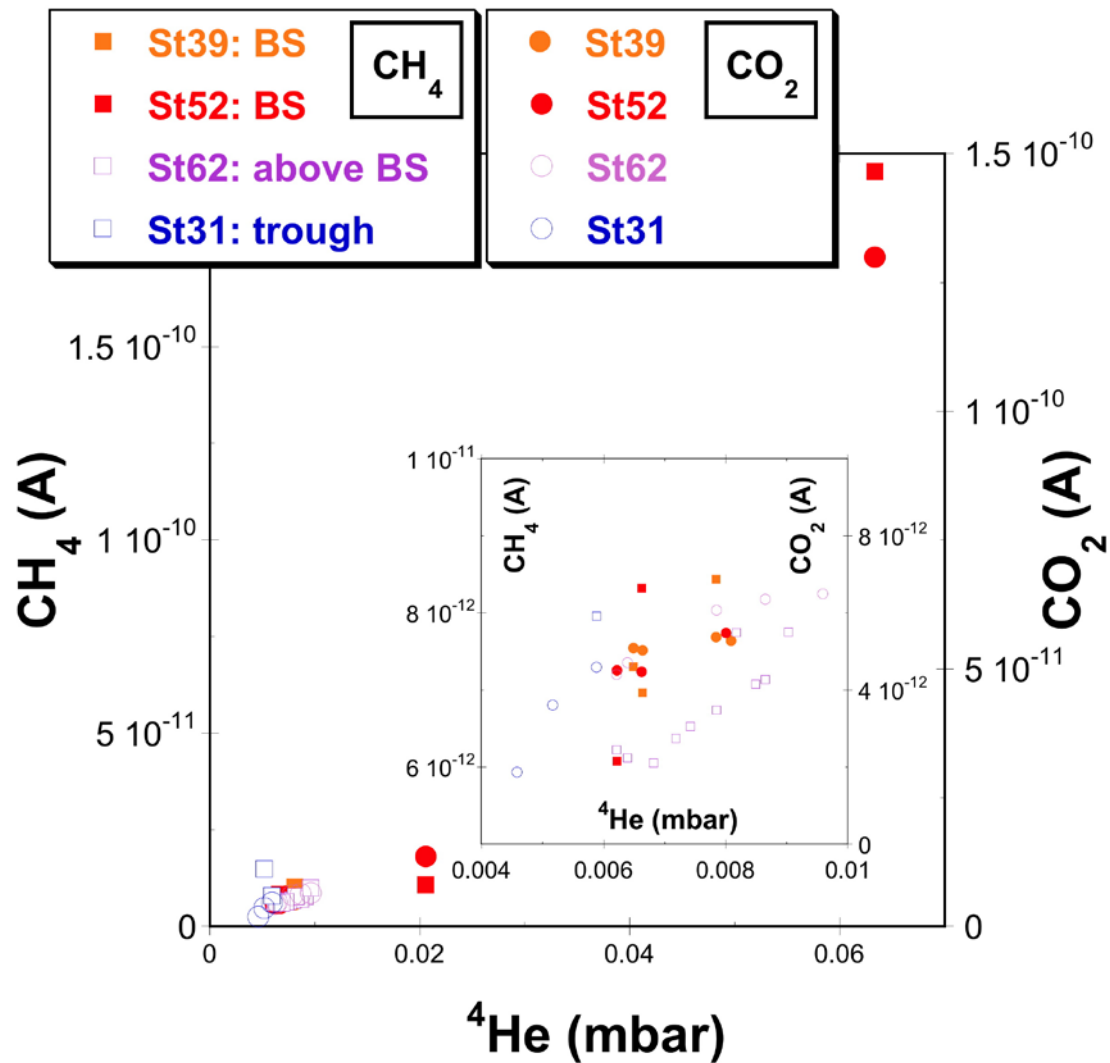


609

610

611 Figure S4: Video still of one of the seven active vents on top of the mound structure.

612



613

614

615 Figure S5: MIMS-determination of dissolved  $^4\text{He}$ ,  $\text{CH}_4$  and  $\text{CO}_2$  partial pressures

616 (mbar) measured at, above and in the vicinity of the hydrothermal vent site (Stxy:

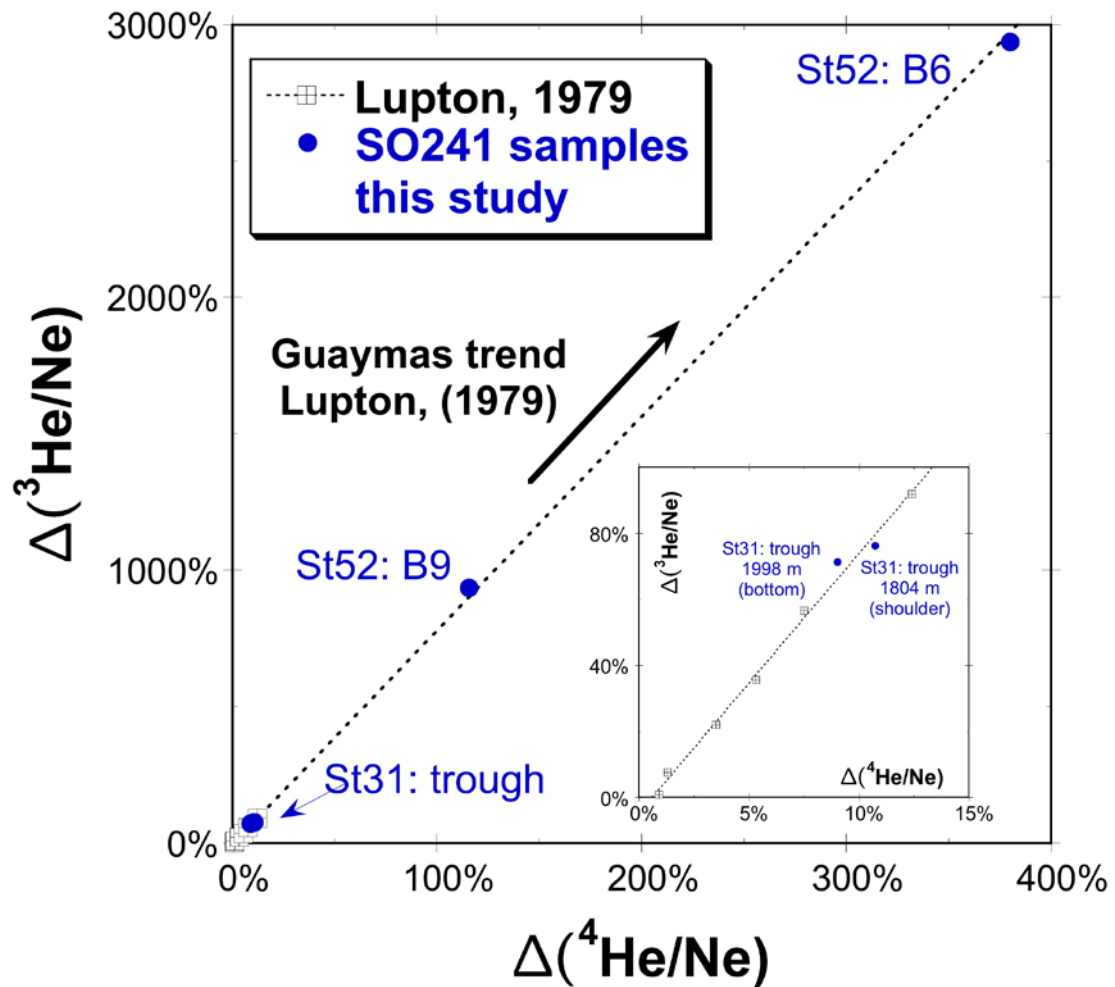
617 station number xy, BS: 'Black Smoker - within the hydrothermal field (stations: 39,

618 52)', above BS: 'free water column above vent sites (station 62)', trough: samples in

619 the deep trough of the northern Guaymas Basin (station 31)).

620 The partial pressures of  $\text{CO}_2$  and  $\text{CH}_4$  are reported as un-calibrated raw MIMS

621 detector signals.



622

623

624 Figure S6: Dissolved He and Ne concentrations measured at the hydrothermal vent  
 625 site in comparison to earlier noble gas measurements in the southern part of the  
 626 Guaymas Basin (Lupton, 1979). The samples from the vent site fall on the line  
 627 defined by the earlier measurements from the southern Guaymas Basin and thus carry  
 628 isotopic light He ( ${}^3\text{He}/{}^4\text{He}: 10.8 \cdot 10^{-6}$ , Lupton, 1979) from the same general MORB  
 629 source. For comparison noble gas (isotope) concentrations are reported and  
 630 normalized as in Lupton, 1979:

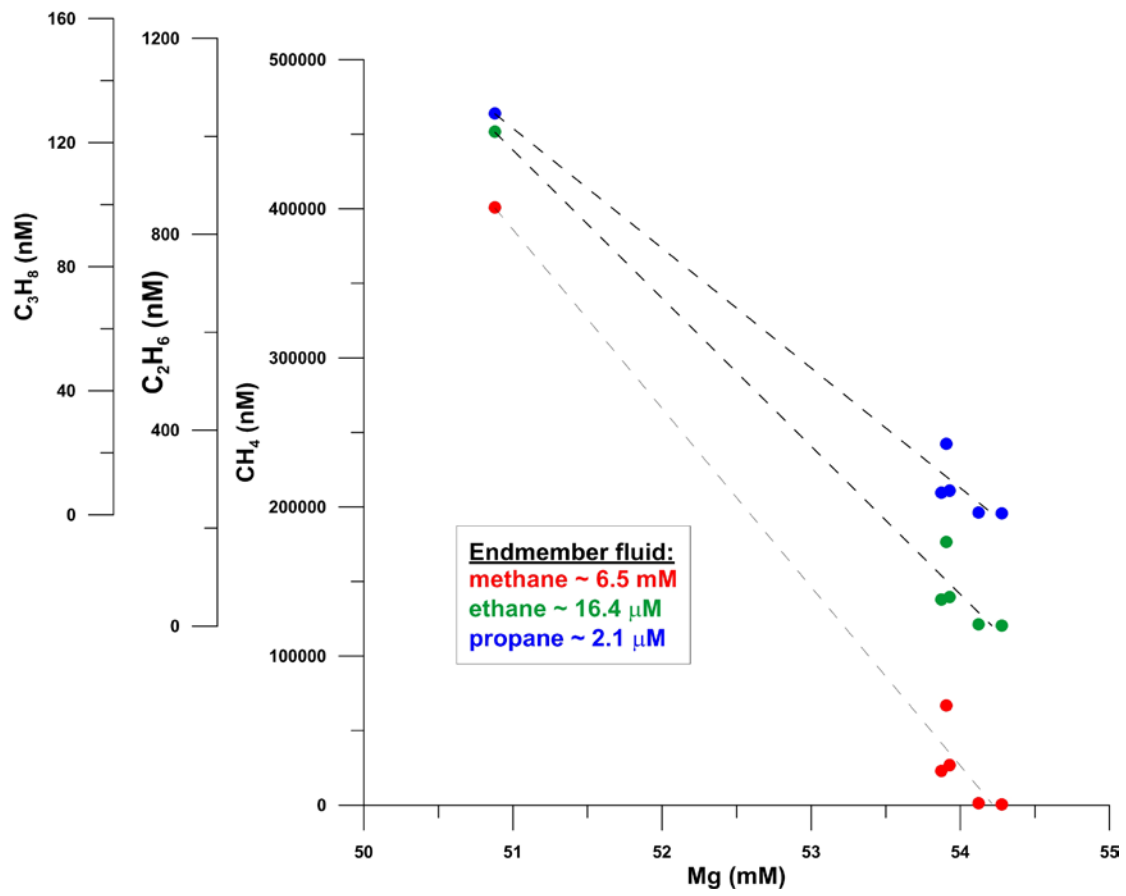
631

632 
$$\Delta\left(\frac{{}^i\text{He}}{\text{Ne}}\right) = \left(\frac{{}^i\text{He}_m}{\text{Ne}_m} \times \frac{\text{He}_{\text{ASW}}}{\text{Ne}_{\text{ASW}}} - 1\right) \times 100 \%$$

633

634 where  $X_m$  depicts the measured concentration of X, and  $X_{ASW}$  is the expected  
635 atmospheric equilibrium concentration (atmospheric saturated water: ASW) for the  
636 given physical condition of the water. As  ${}^1\text{He}_{ASW}$  and  $\text{Ne}_{ASW}$  only barely change with  
637 varying temperature and salinity the  $\text{Ne}_{ASW}/{}^1\text{He}_{ASW}$  ratio is virtually independent of  
638 the actual physical condition of the water. Stxy: 'station number, 'Bz': bottle number.  
639 Station 52: Black Smoker site, Station 31: open water column of the trough.

640



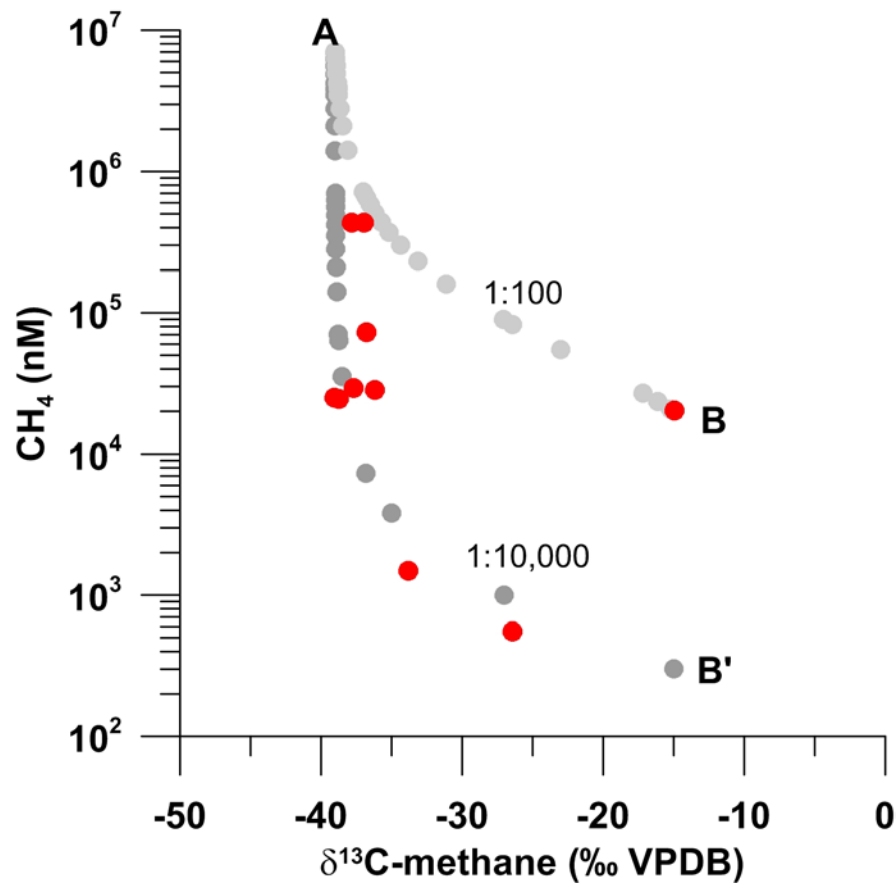
641

642

643 Figure S7: Hydrocarbon end member concentrations (methane, ethane, propane)

644 calculated for hydrothermal fluids venting at the smoker area.

645



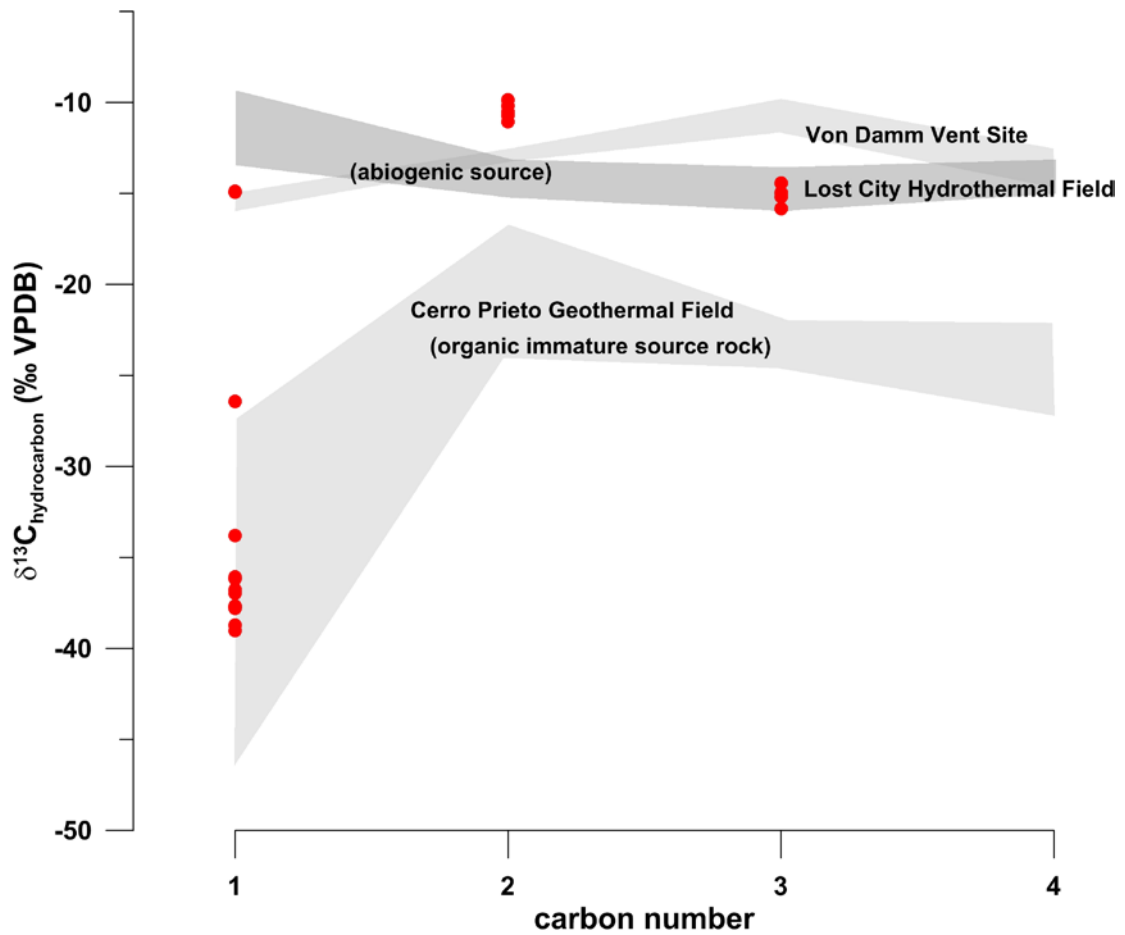
646

647

648 Figure S8: Dissolved methane concentration and carbon isotope data (red dots)  
 649 determined in bottom water samples from the smoker area. Grey dots indicate mixing  
 650 curves of a hydrothermal end member methane A ( $\delta^{13}\text{C} = -39 \text{ ‰}$ , 7nM) with  
 651 admixture of a second methane-containing fluid B and B' ( $\delta^{13}\text{C} = -15 \text{ ‰}$ ),  
 652 respectively, at variable dilution factors of 1:100 and 1:10,000 compared to fluid A.

653

654



655

656

657 Figure S9: Stable carbon isotope composition of hydrocarbons dissolved in venting

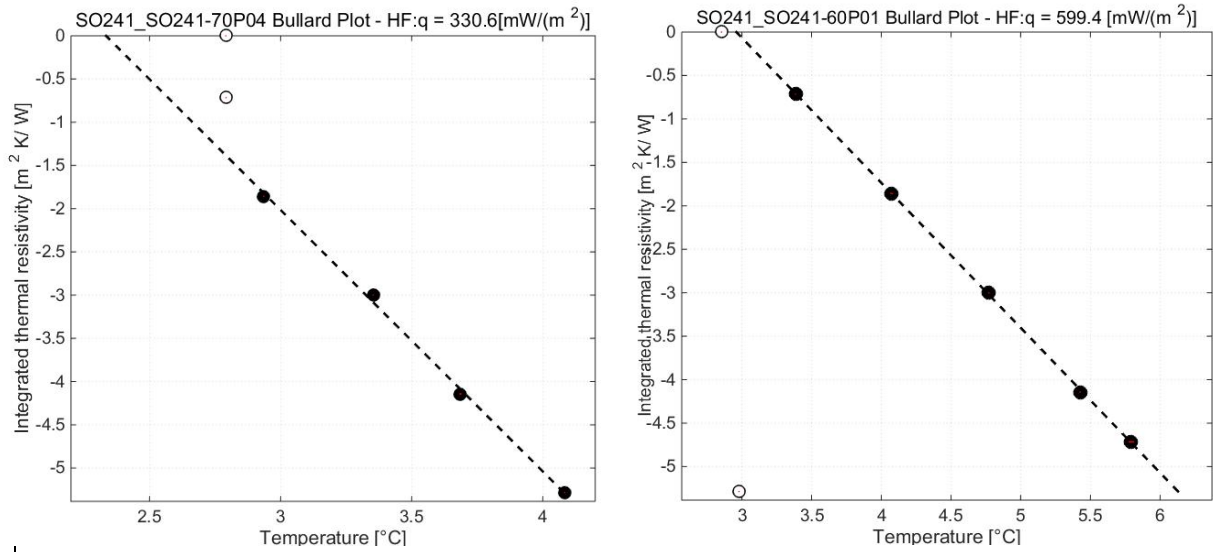
658 hydrothermal fluids (red dots) indicate both hydrocarbons derived from organic

659 matter degradation influenced by volcanic heat intrusion (e.g. Cerro Prieto volcanic

660 complex; Des Marais, 1988), and abiogenic hydrocarbon formation (e.g. Lost City

661 HF, Proskurowski et al., 2008; Von Damm Vent, McDermott et al., 2015).

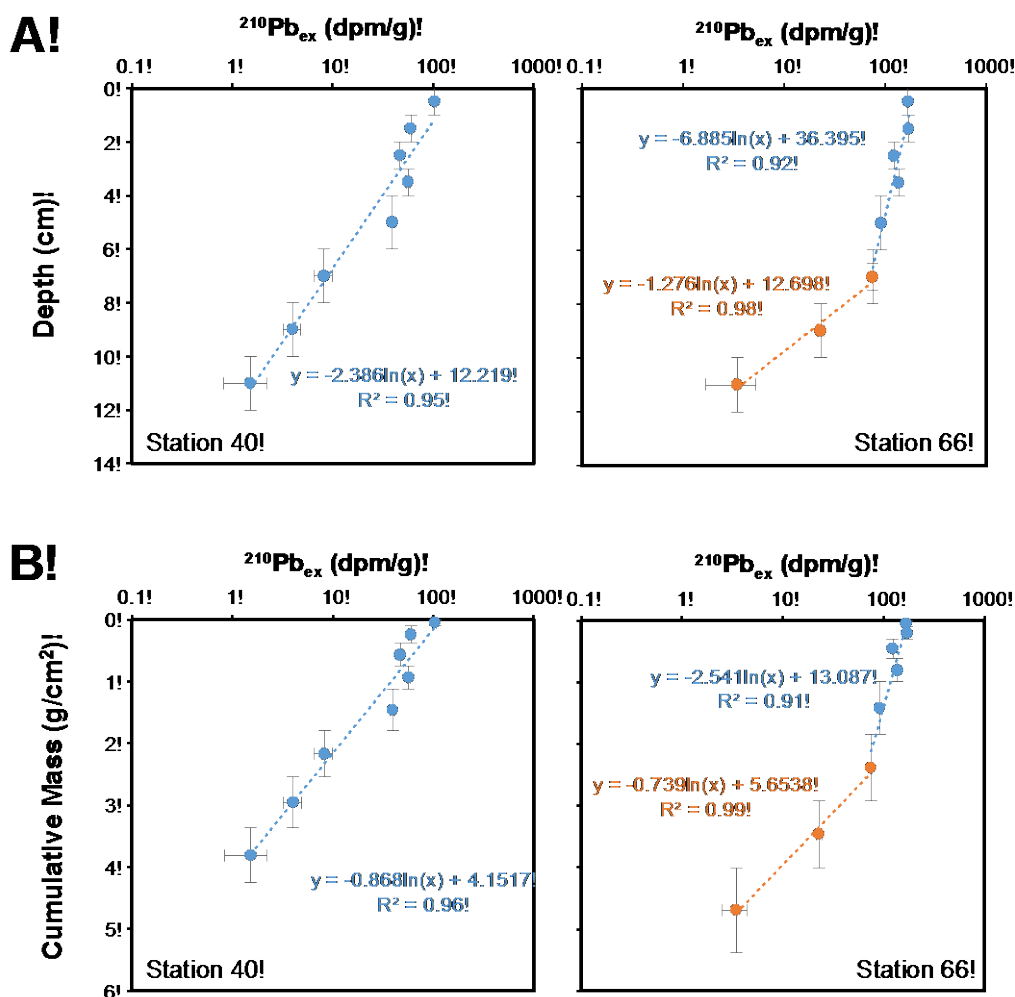




662

663 Figure S10: Calculated heat flow for Site SO241-70P04 (top) and SO241-60P01  
664 (bottom) using the Bullard Plot method. Black dots represent sensors used to calculate  
665 the heat flow whereas unfilled dots represent the sensor positions, which were not  
666 used for any calculations because they were affected by surface artifacts such as  
667 incomplete penetration of the lance.

668



669

670

671 Figure S11:  $^{210}\text{Pb}_{\text{ex}}$  values plotted versus (A) sediment depth and (B) cumulative  
 672 mass at Stations 40 and 66. Lines and equations represent linear-best fit functions and  
 673 their data fit ( $R^2$ ). Station 40 has a good linear fit from the surface to the deepest  
 674 layers sampled, indicating a relatively steady sedimentation rate over the sampling  
 675 interval. By contrast, Station 66 has two best-fit lines, one to match samples from the  
 676 top 6 cm (cyan), and a second one to match samples from 6-12 cm (orange). Samples  
 677 from the top 6 cm at Station 66 show an only minor decrease in  $^{210}\text{Pb}_{\text{ex}}$ , presumably  
 678 due to vertical sediment mixing by macrofauna. The samples from 6-12 cm at Station  
 679 66 show a stronger  $^{210}\text{Pb}_{\text{ex}}$  decrease with depth that more likely reflect the  
 680 sedimentation rate of the site and were thus used for calculations of sedimentation

681 rates. While the profiles of  $^{210}\text{Pb}_{\text{ex}}$  show good agreement independent of the y-axis  
682 units at Station 40, there is a considerable difference between  $^{210}\text{Pb}_{\text{ex}}$  profiles at  
683 Station 66 depending on whether sediment depth or cumulative mass are used as y-  
684 axis units. This discrepancy is likely an artefact of core compaction during sediment  
685 sampling. We consider  $^{210}\text{Pb}_{\text{ex}}$  relationships with cumulative mass, which correct for  
686 compaction effects during coring, to be more reliable (especially at Station 66), and  
687 thus report sedimentation rates that have been corrected for cumulative mass in this  
688 article.

689 *Supplementary Tables*

690 Table S1: Heat flow measurements carried out during SO241

691

Station	Penetration	Latitude	Longitude	Water Depth [m]	Temp. Gradient [K/m]	k [W/mK]	Heat flow [mW/m <sup>2</sup> ]
SO241-51	Pen 01	27° 24.472'	111° 23.377'	1840	11.441	0.739	8069.3
SO241-58	Pen 01	27° 24.487'	111° 23.377'	1837	9.857	0.720	6508.7
SO241-60a	Pen 01	27° 24.623'	111° 23.626'	1834	0.856	0.7 *	599.4
	Pen 02	27° 24.554'	111° 23.512'	1840	2.789	0.7 *	1952.6
	Pen 03	27° 24.273'	111° 23.396'	1840	4.581	0.7 *	3206.1
	Pen 04	27° 24.408'	111° 23.288'	1849	2.039	0.7 *	1427.0
	Pen 05	27° 24.341'	111° 23.177'	1852	1.014	0.7 *	709.6
	Pen 06	27° 24.265'	111° 23.082'	1844	0.737	0.7 *	516.1
	Pen 07	27° 24.193'	111° 22.956'	1834	0.827	0.7 *	578.7
SO241-60b	Pen 01	27° 24.605'	111° 23.317'	1837	0.391	0.7 *	274.0
	Pen 02	27° 24.552'	111° 23.347'	1834	3.451	0.7 *	2415.4
	Pen 04	27° 24.543'	111° 23.351'	1837	15.479	0.7 *	10835.0
SO241-70	Pen01	27° 25.802'	111° 25.486'	1870	0.375	0.7 *	262.2
	Pen02	27° 25.460'	111° 24.946'	2019	0.483	0.7 *	338.1
	Pen03	27° 25.955'	111° 24.493'	2046	0.432	0.7 *	302.6
	Pen 04	27° 24.837'	111° 23.951	2025	0.457	0.7 *	319.7

Thermal conductivities k with an asterisk (\*) are assumed.

692

Table S2: Geochemical data of the water column sampled above the black smoker

Bottle	Latitude	Longitude	Depth	Temperature	Salinity	Methane (C1)	Ethane (C2)	Propane (C3)	$\delta^{13}\text{C-C1}$	$\delta^{13}\text{C-C2}$	$\delta^{13}\text{C-C3}$	$^{222}\text{Rn}_{(\text{exc.})}^{\text{a}}$	Mn	Mg	Sr	$^{87}\text{Sr}/^{86}\text{Sr}$	Si	Ba	Li	
	N	W	(m)	(°C)	(‰)	(nM)	(nM)	(nM)	(‰ VPDB)	(‰ VPDB)	(‰ VPDB)	enrich. fact.	( $\mu\text{mol/l}$ )	(mmol/l)	( $\mu\text{mol/l}$ )		(mmol/l)	(nmol/l)	( $\mu\text{mol/l}$ )	
1	27.41258	-111.3870	1504	3.1	34.60															
2	27.41284	-111.38696	1766	2.9	34.61	1366.1	3.7	0.8	-33.8				0.02	53.0	88.6	0.70917	0.16	128	23.1	
3	27.41288	-111.38696	1767	2.9	34.61							1.7	<d.l.	54.1	88.7	0	0.18	145	24.9	
4	27.41204	-111.38732	1768	4.1	34.55	508.2	0.8	0.4	-26.4				0.14	52.8	88.2		0.18	147	23.3	
5	27.41204	-111.38732	1768	4.1	34.64							1.0	<d.l.	54.3	89.2	7	0.18	143	24.9	
6	27.4121	-111.38732	1768	4.3	34.68	66885.7	171.7	22.9	-36.8	-9.9	-15.8		0.49	52.9	88.4		0.18	451	23.8	
8	27.4121	-111.38732	1768	4.4	34.62							16.2	3.79	53.9	89.6	9	0.26	946	29.0	
9	27.41212	-111.38734	1772	6.9	34.64	26801.6	59.1	7.8	-37.7	-10.5			1.33	53.9	88.6	0.70915	0.20	410	26.5	
						26010.5	57.4	8.2	-36.2							6				
10	27.41214	-111.3872	1775	17.4	34.96	22987.6	54.2	7.1	-39.0	-11.1			1.18	53.9	88.9	0.70915	0.20	383	26.3	
						22466.2	52.1	6.8	-38.7			4.5				9				
11	27.41214	-111.3872	1775	28.0	34.17	18684.1	42.6	6.1	-14.9	-10.7	-14.4		1.10 <sup>b</sup>	52.9 <sup>b</sup>	88.3 <sup>b</sup>		0.19 <sup>b</sup>	353 <sup>b</sup>	24.7 <sup>b</sup>	
									-14.9											
12	27.41212	-111.38718	1773	12.1	34.26	360284.0	849.3	137.4		-10.2	-15.0									
						400801.8	1009.3	129.4	-37.0			81.5	23.9	51.0	90.6	0.70890	0.69	1766	59.2	
									-37.8							6				

<sup>a</sup>Enrichment factor of  $^{222}\text{Rn}$  relative to the lowest value measured on this CTD station (bottle 5). See text for details.

<sup>b</sup>Inorganic geochemistry values are a mixture of bottle 10 (~20%) and bottle 11 (~80%)

695 Table S3: Isotope ratios of He and Ne reported as the percentage deviations of  $^3\text{He}/\text{Ne}$  and  
 696  $^4\text{He}/\text{Ne}$  from the solubility ratios (see Lupton (1979) for details).  
 697

<b>Location</b>	<b>Bottle</b>	<b>Latitude</b>	<b>Longitude</b>	<b><math>\Delta(^3\text{He}/\text{Ne})</math> [%]</b>	<b><math>\Delta(^4\text{He}/\text{Ne})</math> [%]</b>
		N	W		
Black Smoker	6	27.4121	-111.38732	2937	380
Black Smoker	9	27.41212	-111.38734	936	116
Background trough bottom	2	37.30207	-111.52433	71	9
Background trough shoulder	7	37.30207	-111.52433	76	11

698  
 699